Cavity dynamics in water entry at low Froude numbers

HONGMEI YAN, YUMING LIU, JAKUB KOMINIARCZUK AND DICK K. P. YUE†

Department of Mechanical Engineering, Massachusetts Institute of Technology,
Cambridge, MA 02139, USA

The dynamics of the air cavity created by vertical water entry of a three-dimensional body is investigated theoretically, computationally and experimentally. The study is focused in the range of relatively low Froude numbers, $F_r \equiv V(gD)^{-1/2} \leqslant O(10)$ (where V is the dropping velocity of the body, D its characteristic dimension and g the gravitational acceleration), when the inertia and gravity effects are comparable. To understand the physical processes involved in the evolution of cavity, we conduct laboratory experiments of water entry of freely dropping spheres. A matched asymptotic theory for the description of the cavity dynamics is developed based on the slender-body theory in the context of potential flow. Direct comparisons with experimental data show that the asymptotic theory properly captures the key physical effects involved in the development of the cavity, and in particular gives a reasonable prediction of the maximum size of the cavity and the time of cavity closure. Due to the inherent assumption in the asymptotic theory, it is incapable of accurately predicting the flow details near the free surface and the body, where nonlinear free surface and body boundary effects are important. To complement the asymptotic theory, a fully nonlinear numerical study using an axisymmetric boundary integral equation is performed. The numerically obtained dependencies of the cavity height and closure time on Froude number and body geometry are in excellent agreement with available experiments.

Key words: bubble dynamics, collisions with walls/surfaces, wave–structure interactions

1. Introduction

The entry of a solid into water or other liquids gives rise to a sequence of complex events. Research work on this subject has been mainly focused on the following two areas: (i) prediction of impact loads on the body at the initial stage of water entry; and (ii) understanding of the evolution of the air cavity behind the falling body after the initial impact. The focus of this paper is on the second problem, and for relatively low Froude numbers where both inertia and gravity effects are of relevance.

The dynamics of water impact and air cavities was considered by Worthington & Cole (1900). The study on this subject was intensified during World War II for the design of military projectiles entering water at high speed (Gilbarg & Anderson 1948; May & Woodhull 1948; Richardson 1948; May 1951, 1952). Most of these early studies

† Email address for correspondence: yue@mit.edu

were experimental and focused on high Froude numbers, for which the gravity effect is relatively unimportant. Due to basic scientific interest and practical importance, recent studies have expanded to relatively low Froude numbers, where gravity effects are comparable to inertia effects. An important application in naval architecture is the large hydrodynamic loads on surface ships and offshore structures due to water entry/impact as a result of large-amplitude relative motions (e.g. Greenhow 1988; Korobkin & Pukhnachov 1988). The formation of air cavity also significantly influences the dynamics and trajectory of low-speed projectiles such as mines deployed from ships or airplanes (e.g. Chu *et al.* 2004; Holland *et al.* 2004). On a much smaller scale, the water impact and subsequent cavity evolution play an important role in the locomotion of water animals such as shore birds and lizards (e.g. Laerm 1974; Glasheen & McMahon 1996).

In addition to experiments, there are also theoretical and numerical studies of the air cavity dynamics associated with water entry. Two-dimensional analytic models were used to study the cavity dynamics by Birkhoff & Zarantonello (1957) and Lee, Longoria & Wilson (1997). Because a cavity cannot form in two-dimensional potential flow, they have to introduce an arbitrary constant to make the (two-dimensional) kinetic energy finite and, in effect, account for three-dimensional flow effects. The value of this constant was determined by fitting the theoretical prediction with experimental data and/or nonlinear numerical simulations. Duclaux *et al.* (2007) developed an analytical model for the time evolution of the cavity based on the Besant–Rayleigh equation. In this model, arbitrary coefficients are also introduced in determining the kinetic energy of the fluid in the expansion phase of the cavity and to model three-dimensional flow effects. These coefficients are again fitted against experimental measurements. There are no theoretical models so far that do not require the use of such empirical coefficient(s). Owing to complexity of the unsteady nonlinear flow, numerical studies on the cavity dynamics associated with water entry are limited. Gaudet (1998) performed a fully nonlinear potential flow simulation of water entry of circular disks at low Froude numbers using a boundary-integral method with constant panels. His numerical results are in good agreement with the measurements of Glasheen & McMahon (1996).

In this work, we investigate the problem of air cavity dynamics in the water entry of bodies at relatively low Froude numbers. We perform matched asymptotic analysis, fully nonlinear numerical simulations, and also laboratory experiments. For simplicity, we consider vertically axisymmetric bodies in normal incidence. The theoretical analysis and numerical computation are based on the potential-flow formulation (§ 2). An analytic solution is developed, based on the slender body assumption, for the cavity evolution until pinch-off (§ 3). Unlike existing theoretical models, by using matched asymptotic analysis, the present solution is complete in the sense that it does not contain any arbitrary constant or fitting parameter. To understand the detailed flow characteristics near the free surface and in the neighbourhood of the body where the asymptotic solution is less valid, we perform fully nonlinear simulations using a mixed Eulerian–Lagrangian (MEL) boundary-integral equation method based on (axisymmetric) ring sources (§ 4.1). Laboratory experiments involving dropping of billiard balls into water are conducted (§ 4.2) to provide direct comparisons to the asymptotic theory and numerical simulations. The cavity dynamics and evolution and their dependencies on Froude number are studied for the sphere and contrasted against those for a variety of other body shapes (§ 5). Overall, potential-flow-based formulation appears to adequately describe the cavity dynamics up till the moment of pinch-off. In particular, the matched-asymptotic theory gives reliable predictions of the cavity closure time (T) and total cavity height (H) as a function of the
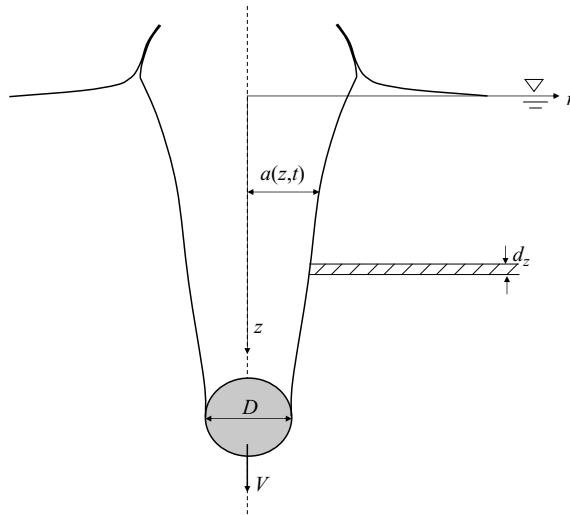
FIGURE 1. Schematic of an air cavity created by the vertical water entry
of an axisymmetric body.

Froude number. On the other hand, the fully nonlinear simulations provide important details associated with the cavity shape and the free surface evolution. We conclude in §6.

2. Problem statement

2.1. *The initial boundary value problem*

We address the hydrodynamic problem of air cavity development in vertical water entry of an axisymmetric body with relatively low Froude numbers, $F_r \equiv V(gD)^{-1/2} \leqslant O(10)$, where V is the characteristic dropping velocity of the body, D the characteristic length of the body and g the gravitational acceleration. For relatively large bodies and speeds, and short evolution time, we neglect viscosity and surface tension (which might be of importance near cavity closure), and assume a smooth hydrophobic body surface. The problem is then governed by the Froude number F_r (and body geometry and body relative density). For simplicity, we restrict ourselves to the case of a vertically axisymmetric body and normal incidence, and assume that the resultant flow is also (approximately) axisymmetric.

We define axisymmetric cylindrical coordinate system $\boldsymbol{x} \equiv (z, r)$ where z is the vertical coordinate positive downwards, and r the radial coordinate. The origin is on the undisturbed free surface (see figure 1).

Assuming that the fluid motion is irrotational, the velocity is described by a potential ϕ which satisfies Laplace's equation in the fluid domain $\mathscr{V}$:

$$\nabla^2 \phi(\boldsymbol{x}, t) = \frac{\partial^2 \phi}{\partial r^2} + \frac{1}{r} \frac{\partial \phi}{\partial r} + \frac{\partial^2 \phi}{\partial z^2} = 0, \quad \boldsymbol{x} \in \mathscr{V}(t). \tag{2.1}$$

On the free surface $S_F(\boldsymbol{x}, t)$ which includes the wall of the cavity, ϕ satisfies the kinetic boundary condition, which in Lagrangian form is

$$\frac{\mathrm{D}\boldsymbol{x}}{\mathrm{D}t} = \nabla\phi, \quad \text{on } S_F(\boldsymbol{x}, t) \tag{2.2}$$

where $\mathrm{D}/\mathrm{D}t \equiv \partial/\partial t + \nabla\phi\cdot\nabla$. The dynamic boundary condition on $S_F(\boldsymbol{x}, t)$ in Lagrangian form is

$$\frac{\mathrm{D}\phi}{\mathrm{D}t} = \frac{1}{2}|\nabla\phi|^2 + gz - P_F, \quad \text{on } S_F(\boldsymbol{x}, t), \tag{2.3}$$

where P_F is the pressure on $S_F(\boldsymbol{x}, t)$. Unless the impact speed is very high, aerodynamic effects are small, and we set P_F to be equal to the atmospheric pressure which is constant in this study. This should be valid before cavity closure which is the main objective of this study. (After cavity closure, the pressure on the cavity surface may become time dependent, see e.g. Wang 2004). On the (wetted) body boundary, $S_B(\boldsymbol{x}, t)$, the normal velocity of the flow is specified,

$$\nabla\phi\cdot\boldsymbol{n} = V(t)n_z, \quad \text{on } S_B(\boldsymbol{x}, t), \tag{2.4}$$

where $\boldsymbol{n} \equiv (n_z, n_r)$ is the unit normal pointing out of the fluid, and $V(t)$ is the body velocity which is in general a function of time. In addition, a far-field condition

$$\nabla\phi \to 0, \quad \text{for } |\boldsymbol{x}| \to \infty \tag{2.5}$$

is imposed. At initial time, $t = 0$, the body is just touching the undisturbed free surface on which we impose the initial condition:

$$\phi = 0, \quad \text{on } S_F(\boldsymbol{x}, t = 0). \tag{2.6}$$

The above equations define the initial boundary value problem for ϕ.

If the body drops freely in the water, its motion is governed by the equation of motion:

$$Mg + F(t) = M\frac{\mathrm{d}V(t)}{\mathrm{d}t}, \tag{2.7}$$

where M is the mass of the body and $F(t)$ the total (hydrodynamic plus hydrostatic) force

$$F(t) = \int_{S_B(t)} pn_z \,\mathrm{d}s, \tag{2.8}$$

where the pressure p on the wetted body surface is given by Bernoulli equation

$$\frac{p}{\rho} = -\frac{\partial\phi}{\partial t} - \frac{1}{2}|\nabla\phi|^2 + gz. \tag{2.9}$$

2.2. *Physical insight*

Before we carry out the detailed asymptotic analysis and nonlinear computation, it is helpful to obtain a heuristic understanding of the cavity development and evolution. The water entry of a body and the subsequent cavity evolution behind consist of two main phases. Assuming a constant dropping velocity V, the body position $z_b(t)(> 0)$ after initial impact (at time $t = 0$) is $z_b = Vt$. At some height z_0, the cavity begins to form at $t_0(z_0) = z_0/V$ with an initial radius $a(z_0, t_0) \approx D/2$ where $D/2$ is the body radius (assuming an axisymmetric body). Initially, the cavity expands ($\partial a/\partial t > 0$ for $t > t_0(z_0)$) as the body continues to descend below z_0. After some expansion time $\delta t_1(z_0)$, the cavity reached maximum radius, $a(z_0, t_0 + \delta t_1) = R_m(z_0)$, and then starts to contract, eventually collapsing the cavity. There is generally a height $z = H_c$ at which the cavity first closes, at closure time $t = T$, when $a(H_c, T) = 0$. This initial cavity closure can occur above the free surface ('surface closure', $H_c < 0$) or below the free surface ('deep closure' or 'pinch-off', $H_c > 0$) depending on the value of the Froude

number. Deep closure usually occurs for relatively low Froude numbers, while surface closure generally occurs for larger Froude numbers (Birkhoff & Zarantonello 1957).

For the contraction phase, a heuristic estimate of closure time at any height z_0 can be obtained by assuming steady state, with a constant radial velocity approximated by Bernoulli equation, $-\partial a/\partial t = u(z_0) = (2gz_0)^{1/2}$ for $t > t_0 + \delta t_1$. The time of collapse at z_0, $t_c(z_0) = t_0 + \delta t_1 + \delta t_2$, can be estimated by $\delta t_2(z_0) \simeq 0.5D/u(z_0)$. For some body shapes (e.g. a long vertical cylinder), the expansion phase is short compared to the collapsing phase, $\delta t_1 \ll \delta t_2$. Under this condition, one may neglect δt_1 to obtain the closure time, $T = \min_{z_0} [t_0(z_0) + \delta t_2(z_0)]$. Substituting the value of δt_2 in terms of z_0, we finally obtain $TV/D \simeq (3/2^{5/3})F_r^{2/3}$, corresponding to a pinch-off position $z = H_c = H/3$, where $H = TV$ is the total cavity height at pinch-off time $t = T$. (Details of this can be found in Mann 2005 and Mann *et al.* 2007.)

Despite the simple model, the above estimate obtains good agreement with measurements in the case of relatively long vertical cylinders (Duclaux *et al.* 2007), and remarkably for the case of a sphere entering into soft sand (Lohse *et al.* 2004). For general body shapes, however, the heuristic estimate fails. For example, experimental data show an almost linear dependence of TV/D and H/D on F_r, and $H_c \simeq H/2$, for water entry of circular disks (entering normally) (Glasheen & McMahon 1996) and spheres (Duclaux *et al.* 2007).

3. Asymptotic theory

To understand the basic mechanism governing the evolution of air cavity in water entry of a body, we derive an asymptotic solution of the above problem by assuming the diameter of the cavity d small relative to its length h (e.g. at $F_r \approx 5.0$, $d/h \approx 0.14$ for spheres Duclaux *et al.* 2007 and $d/h \approx 0.12$ for circular disks Glasheen & McMahon 1996 near cavity closure). Of particular interest is the dependence of key cavity dynamics parameters such as closure time and cavity height on the Froude number.

3.1. *Governing equations*

We define a slenderness parameter, $d/h = \varepsilon \ll O(1)$, where d is the characteristic diameter of the cavity, and h its characteristic length. Based on $\varepsilon \ll O(1)$, in the near field of the cavity, the flow is two-dimensional:

$$\frac{\partial \phi}{\partial z} \ll \frac{\partial \phi}{\partial r}, \quad r/h = O(\varepsilon). \tag{3.1}$$

The Laplace equation (2.1) reduces to

$$\frac{\partial^2 \phi}{\partial r^2} + \frac{1}{r}\frac{\partial \phi}{\partial r} = 0, \quad r \ll h, \tag{3.2}$$

and (2.2) on the cavity wall, $r = a(z, t)$, can be rewritten as

$$\frac{\partial a}{\partial t} = \phi_r - \phi_z \frac{\partial a}{\partial z}, \quad \text{at } r = a(z, t). \tag{3.3}$$

To leading order, (3.3) becomes

$$\frac{\partial a}{\partial t} = \phi_r + O(\varepsilon), \quad \text{at } r = R. \tag{3.4}$$

We point out that (3.4) is now applied on a fixed radius $R \ll h$. In practice, R can be chosen to be, say, the (maximum) radius of the body. Similarly, the leading order

dynamic boundary condition (2.3) can also be written simply as

$$\frac{\partial \phi}{\partial t} = gz + O(\varepsilon), \quad \text{at } r = R. \tag{3.5}$$

For relatively large $F_r(> O(1))$ and short cavity evolution time, we ignore wave and splash effects and assume a flat free surface with the boundary condition:

$$\phi(0, r, t) = 0, \quad \text{at } z = 0. \tag{3.6}$$

In the far field of the cavity ($r/h \geqslant O(1)$), the flow is three dimensional with ϕ satisfying (2.1) and (2.5), and the free-surface boundary condition (3.6).

We follow a standard matched asymptotic approach (Van Dyke 1964; Mei, Stiassnie & Yue 2005; Wang 2005, 2007). To account for the effect of cavity wall motion on the flow, we distribute a line source with unknown strength $q(z, t)$ along the centreline of the cavity. The presence of the (finite) body can be accounted for by a moving point source with strength $\sigma(t)$. To satisfy the zero Dirichlet condition (3.6), negative images of the line source and point source with respect to $z = 0$ need to be added. For later reference, to define the velocity potentials ϕ_c and ϕ_b associated respectively with the cavity $q(z, t)$ and the body $\sigma(t)$, and write the total velocity potential as

$$\phi(z, r, t) = \phi_b + \phi_c. \tag{3.7}$$

The body potential can be obtained by choosing $\sigma(t)$ to satisfy (2.4).

The matched asymptotic solution follows standard procedure: (a) obtain the inner and outer expressions of ϕ_c, ϕ_{in} and ϕ_{out} satisfying respectively (3.2), (3.4), (3.5) and (2.1) and (2.5); (b) obtain the outer and inner expansions of ϕ_{in} and ϕ_{out} respectively in an overlap region $\varepsilon h \ll r \ll h$ (far from the cavity in the inner region but close to the body in the outer region) and (c) match these to determine the complete ϕ_c.

3.2. Determination of ϕ_b

We place a moving three-dimensional point source of strength $\sigma(t)$ at cavity (or body centroid) depth $h(t)$. The velocity potential of this point source and its negative image above $z = 0$ is

$$\phi_b(z, r, t) = -\frac{\sigma(t)}{4\pi} \frac{1}{\sqrt{(h-z)^2 + r^2}} + \frac{\sigma(t)}{4\pi} \frac{1}{\sqrt{(h+z)^2 + r^2}}. \tag{3.8}$$

A conceptually clear way to specify the strength $\sigma(t)$ is to use ϕ_b in (3.7) to account for the *vertical* volume flux due to the body. Thus the value of $\sigma(t)$ for (3.8) is obtained by matching the vertical volume flux across the wetted body surface S_B given by (2.4) to that across the front ($z > h$) portion of the Rankine half body formed by the single point source (this flux equals 0.36σ which we shall simply approximate as $\sigma/3$ below). For the sphere, S_B depends on the (assumed) location of the detachment line, which, if we specify it to be at maximum radius, say, obtains $\sigma(t) = 2\pi R^2 V(t)$. For the inverted truncated cone in §5.2, the separation line is at the top edge, yielding $\sigma(t) = 3\pi R^2 V(t) \sin(\theta/2)$, where θ is the cone vertex angle. The circular disk is simply the limit of $\theta = \pi$ giving $\sigma(t) = 3\pi R^2 V(t)$. We remark that the decomposition (3.7) in principle leaves some freedom in the specification of σ in (3.8). The present choice which frees ϕ_c from satisfying the vertical flux due to the body is a theoretically elegant one, and, as we shall show in §5, gives remarkably good predictions relative to fully nonlinear simulations and experiments.

3.3. *Determination of ϕ_c*

For the inner solution, the problem is two-dimensional, and the velocity potential due to line source (and its negative image) can be written as

$$(\phi_c)_{in}(z, r, t) = \frac{q(z, t)}{2\pi} \log\left(\frac{r}{2h}\right) + f_1(z, t), \quad r \ll h, \tag{3.9}$$

where the source strength $q(z, t)$ is unknown. The function $f_1(z, t)$ is also unknown, to be determined by later asymptotic matching.

The outer problem is three-dimensional, and ϕ_c can be expressed as that due to a three-dimensional line source (and its negative image):

$$(\phi_c)_{out}(z, r, t) = -\int_{-h}^{h} \frac{q(\xi, t)}{4\pi} \frac{1}{\sqrt{(\xi - z)^2 + r^2}} \, d\xi. \tag{3.10}$$

Equation (3.10) has an inner expansion for $r/h \ll 1$ which has the form of (3.9) (see e.g. Newman 1977) but with $f_1(z, t)$ given by

$$f_1(z, t) = \frac{1}{4\pi} \int_{z}^{h} \frac{\partial q(\xi, t)}{\partial \xi} \log[2(\xi - z)/(2h)] \, d\xi - \frac{1}{4\pi} \int_{-h}^{z} \frac{\partial q(\xi, t)}{\partial \xi} \log[2(z - \xi)/(2h)] \, d\xi. \tag{3.11}$$

Note that with this matching, the potential ϕ_c in the whole fluid domain is uniquely specified in terms of the unknown line source $q(z, t)$.

To determine $q(z, t)$, we impose the dynamic boundary condition (3.5) for the total inner solution

$$\phi_{in}(z, r, t) = (\phi_c)_{in} + \phi_b. \tag{3.12}$$

Upon integrating (3.5) with respect to time, we obtain

$$\phi_{in}(z, R, t) = gz(t - t_0(z)) + C(z) \tag{3.13}$$

where $t_0(z)$ is the time when the body arrives at the depth z, i.e. $z = \int_0^{t_0} V(t) \, dt$.

In (3.13), the integration constant $C(z)$ given by the velocity potential on the cavity wall at z at $t = t_0$:

$$C(z) = \phi_{in}(z, R, t_0) = \phi_b(z, R, t_0) + f_2(z), \tag{3.14}$$

where

$$\phi_{b0} \equiv \phi_b(z, R, t_0) = -\frac{m(t_0)}{4\pi} \frac{1}{R} + \frac{m(t_0)}{4\pi} \frac{1}{\sqrt{4z^2 + R^2}}, \tag{3.15}$$

$$f_2(z) = f_1(z, t_0) = -\frac{1}{4\pi} \int_{-z}^{z} \frac{\partial q(\xi, t_0)}{\partial \xi} \log[2(z - \xi)/(2z)] \, d\xi. \tag{3.16}$$

At any time $t > t_0$, evaluation of (3.12) at $r = R$ to satisfy (3.13) gives an integral equation for the unknown $q(z, t)$:

$$q(z, t) = \frac{-2\pi}{\log(2h/R)} \{gz(t - t_0) - \phi_b + \phi_{b0} - f_1(z, t) + f_2(z)\}\bigg|_{r=R}, \quad t > t_0. \tag{3.17}$$

Equation (3.17) can be solved to $O(\varepsilon^2)$ by substituting into (3.17) an expansion for $q(z, t)$ of the form

$$q(z, t) = q_0(z, t) + q_1(z, t) + O(\varepsilon^2), \quad t > t_0 \tag{3.18}$$

where $q_0 = O(1)$ and $q_1 = O(\varepsilon)$. The functions $q_0(z, t)$ and $q_1(z, t)$ are obtained successively to yield

$$q_0(z, t) = \left. \frac{-2\pi}{\log(2h/R)} \{gz(t - t_0) - \phi_b + \phi_{b0}\} \right|_{r=R}, \qquad (3.19a)$$

$$q_1(z, t) = \left. \frac{-2\pi}{\log(2h/R)} \{-f_1(z, t) + f_2(z)\} \right|_{r=R}, \qquad (3.19b)$$

where $q = q_0$ is used in the evaluation of $f_1(z, t)$ and $f_2(z)$ in (3.19b). With the line source strength $q(z, t)$ now known, the velocity potential ϕ is obtained in a closed form.

We remark that in the existing analytic models of Birkhoff & Zarantonello (1957) and Lee *et al.* (1997), a purely two-dimensional (inner) solution is assumed at each depth z (cf. (3.9)). Because this solution is divergent in the far-field, an arbitrary parameter has to be introduced. For example, Birkhoff & Zarantonello (1957) set the maximum radius of the two-dimensional flow to be $15 \sim 30$ times of the cavity radius in the determination of kinetic energy of the two-dimensional flow. The present match-asymptotic treatment and the introduction of the (three dimensional) body source avoids this difficulty and correctly accounts for the full (far field) three-dimensional effect, without any free parameter.

3.4. *Time evolution of the cavity*

The radial velocity of the cavity is

$$\phi_r = (\phi_c)_r + (\phi_b)_r = \frac{q(z, t)}{2\pi r} + \frac{\partial \phi_b}{\partial r}, \quad \text{at } r = R. \qquad (3.20)$$

The radius $a(z, t)$ of the cavity can be evaluated by integrating (3.4) with respect to t:

$$a(z, t) = R + \int_{t_0}^{t} \phi_r \, dt, \quad t > t_0. \qquad (3.21)$$

The decomposition (3.7) now allows us to obtain a clear qualitative description of the phases of cavity development discussed in §2.2: (a) For small $(t - t_0)V/R$, at any depth z_0, $q \sim q_0 \sim (t - t_0)$ from (3.19a), and $(\phi_b)_r$ dominates the radial velocity (3.20). Since $(\phi_b)_r > 0$ from (3.8) (for $\sigma(t) > 0$), this accounts for the initial expansion phase of the cavity at this depth. (b) As $t - t_0$ increases, it can be shown from (3.19a) (and (3.19b)) that $q(z_0, t) < 0$ (so that $(\phi_c)_r < 0$) for $(t - t_0) \gtrsim VR/(gz_0)$, with a magnitude that increases with $t - t_0$. In the meantime, $(\phi_b)_r \sim (t - t_0)^{-3}$ decreases, so that at some time $t = t_0 + \delta t_1(z_0)$, the two competing contributions balance, at the point when the cavity reaches maximum radius $R_m(z_0)$. (c) For $t > t_0 + \delta t_1(z_0)$, ϕ_r reverses sign (dominated by $(\phi_c)_r$), and the cavity eventually collapses at this location using time $t_c - t_0 - \delta t_1 = \delta t_2(z_0)$.

At depth z_0, $\delta t_1(z_0)$ is determined from setting $\phi_r = 0$ in (3.20); and $R_m(z_0)$ from (3.21) with $t = t_0(z_0) + \delta t_1(z_0)$. The time of collapse, $t_c(z_0) = t_0 + \delta t_1(z_0) + \delta t_2(z_0)$ is then the upper limit of the integral to t_c in (3.21) to obtain $a = 0$. Finally, the closure time of the cavity itself T is defined as the minimum of $t_c(z_0)$ over all z_0 of the cavity, given by

$$\left. \frac{dt_c(z_0)}{dz_0} \right|_{z_0 = H_c} = 0, \qquad (3.22)$$

where $z_0 = H_c$ is the depth at which this (first) pinch-off occurs. The total cavity height H at this closure time T is simply $\int_0^T V \, dt$.

3.5. *Evaluation of the hydrodynamic drag*

For later reference, for the case of freely falling bodies, it is necessary to determine the hydrodynamic (drag) force on the body. The drag force on the body $F(t)$ can be evaluated in terms of the rate at which total energy E is imparted into the fluid at that time, which is in principle now known (from §3.3). One approach leading to an approximation can be obtained by accounting for this energy in terms of the total energy in the two-dimensional plane $E_{2D}(z)$:

$$E(t) = \int_0^{z_b(t)} E_{2D}(z, t)\, dz, \tag{3.23}$$

where $z_b(t)$ is the current position of the body. Thus

$$F(t) = \frac{1}{V}\frac{dE}{dt} = E_{2D}(z_b, t) + \frac{1}{V}\int_0^{z_b(t)} \frac{dE_{2D}}{dt}\, dz. \tag{3.24}$$

We now make the slender body assumption that the energy $E_{2D}(z)$ in each two-dimensional plane is conserved (Birkhoff & Zarantonello 1957), which gives

$$F(t) \approx E_{2D}(z_b, t) \approx \int_0^{R_m(z_b)} (\rho g z_b)2\pi r\, dr = \pi\rho g z_b R_m^2(z_b), \tag{3.25}$$

where the second approximation is obtained from the slender body approximation and equating the total energy E_{2D} to the maximum potential energy of the fluid displaced by the cavity at the current body depth $z_b(t)$.

We note that, in comparing (3.24) and (3.25), it can be seen that the second (neglected) term in (3.24) is generally negative. The reasoning is clear again because of the decomposition (3.7). $E_{2D}(z)$ is due to both ϕ_b and ϕ_c. The contribution due to the line source ϕ_c satisfies approximately slender body assumption (so that the time change at any depth is small). The contribution due to the body source ϕ_b is negative for $z < z_b$ (see (3.8)), so that the net contribution is negative and (3.25) is expected to somewhat overestimate the drag on the body (see figure 5).

4. Numerical simulation and laboratory experiments

4.1. *Fully nonlinear numerical simulation*

The matched asymptotic analysis is not expected to be good for the flow near the free surface or close to the body. To provide an independent check of its validity and to provide a simulation capability for general entry body geometries and Froude numbers we develop here a fully nonlinear numerical method based on an MEL ring-source boundary-integral equation method. The general approach follows closely that of Dommermuth & Yue (1987) and Xue & Yue (1998); for completeness, we outline here the key steps.

The nonlinear initial boundary value problem in §2 is solved in the time domain starting from initial conditions. The problem is solved in the (axisymmetric) z-r plane. At each time, the unknown normal velocities on the trace of the free surface/cavity S_F, ∂S_F, and the unknown velocity potential on the trace of the body surface S_B, ∂S_B, are obtained by solving the integral equation (Dommermuth & Yue 1987):

$$\beta(z, r, t)\phi(z, r, t) = \int_{\partial S_F + \partial S_B} \left(\frac{\partial\phi}{\partial n'} - \phi\frac{\partial}{\partial n'}\right) G(z, r; z', r')r'\, d\ell', \quad (z, r) \in \partial S_F + \partial S_B, \tag{4.1}$$

α_0	$F_r = 3$		$F_r = 5$	
	$T V_0 / D$	H_c / D	$T V_0 / D$	H_c / D
60°	4.38	1.76	7.10	2.74
65°	4.38	1.76	7.09	2.72
70°	4.36 (4.36)	1.74 (1.73)	7.04 (7.03)	2.71 (2.72)
75°	4.32	1.70	6.94	2.68
80°	4.23	1.65	6.78	2.64

TABLE 1. Effect of the flow separation angle α_0 upon the cavity closure time T and closure depth H_c in water entry of a freely falling sphere (§ 5.1) at two Froude numbers ($F_r = 3.0$ and $F_r = 5.0$) obtained by fully nonlinear simulation. The values inside the parentheses are obtained with doubled panel numbers along $\partial S_B + \partial S_F$ and halved time step in the simulation.

where β is the subtended solid angle and $G = \int_0^{2\pi} R^{-1} d\theta'$, $R = [(z - z')^2 + (r - r' \cos \theta')^2 + (r' \sin \theta')^2]^{1/2}$ is the Rankine ring source Green function (Hulme 1983). Because of the transient nature of the problem, the special far-field closure treatments of Dommermuth & Yue (1987) and Xue & Yue (1998) are not important here. On the other hand, the treatment of flow separation from the body must be considered with some care. For bodies with sharp edges or corners (such as the disk or the inverted truncated cone in § 5.2), the separation point (from which the flow leaves tangentially from the body) is well defined.

For general smoothed geometries such as spheres, the separation point may be affected by the Froude number and body surface properties (Duez *et al.* 2007). In the numerical method, the separation position may be determined based on the requirement of satisfying both the free-surface and body boundary conditions, but sensitively depends on numerical resolution (e.g. Dommermuth & Yue 1987; Liu, Xue & Yue 2001). For the present problem, the separation point is observed in the experiments to be relatively invariant during the development of cavity. Thus, in this study, we presume the separation angle α_0 (measured from the downward vertical) and assume the flow detaches the body surface (at $\alpha = \alpha_0$) tangentially. Table 1 shows the dependence of cavity closure time and closure depth on prescribed value of separation angle α_0 for a freely falling sphere for two different F_r values (§ 5.1). The results indicate that the key cavity closure parameters are relatively insensitive to α_0 in the low-Froude-number range. For a horizontal circular cylinder impact, Lin & Shieh (1997) observed that the separation point remains unchanged after separation with $\alpha_0 = 70° \sim 80°$ for $F_r = O(1)$. In water entry of small hydrophobic spheres, Aristoff & Bush (2009) found that $\alpha_0 = 70° \sim 80°$ for $F_r = O(10^{-1}) \sim O(10^2)$. Based on the above, we set $\alpha_0 = 70°$ in this study for the sphere entry problem.

Finally, we comment on the numerics. For axisymmetric problems, the present method requires discretization only along a (one-dimensional) line. In this study, we typically use 40 panels along ∂S_B, 300 panels on ∂S_F and dimensionless time step $\triangle t = 0.005$. With these parameters, the numerical errors are converged to less than 1 %. Table 1 shows a sample convergence result with two discretizations. (Extensive convergence tests and numerical validations can be found in Dommermuth & Yue 1987 and Xue & Yue 1998.)

4.2. *Freely falling sphere experiments*

We conduct laboratory experiments of water entry of freely falling spheres. Of special interest in the present context are the salient features of the cavity shapes
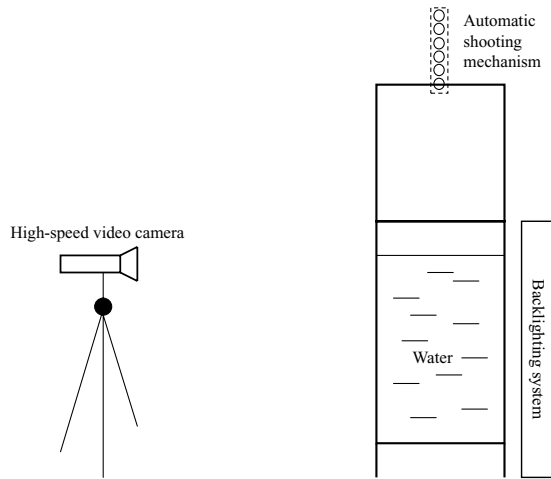
FIGURE 2. Sketch of the experimental set-up.

and development (for $F_r \lesssim O(10)$). Details of the experimental effort are given in Kominiarczuk (2007) (the experimental set-up is similar to that of Truscott & Techet 2009). The experiment is conducted in a water tank 0.9 m wide, 1.5 m long and 1.8 m deep, as shown in figure 2. Standard billiard balls, diameter 5.72 cm, made of phenolic resin ($\rho_b/\rho \approx 1.73$) are dropped from different heights above the still water level corresponding to $F_r = 3 \sim 7$. The cavity development after water entry is recorded by high-speed video camera at up to 2100 frames per second at 50 µs exposure (typical dimensional $T \sim 0.1$ s) captured at a resolution of 800 (vertical) by 350 (horizontal) pixels in a (vertical) field of view of 0.4 m (dimensional H is between $0.2 \sim 0.4$ m for our Froude number range).

5. Results

5.1. *Freely falling spheres*

We compare asymptotic theory, nonlinear simulation and laboratory experiments with special focus on the evolution of the kinematics and profile of cavity wall, and the dependence of closure time and pinch-off height on Froude number, for a free falling sphere, diameter D and initial velocity at water impact V_0.

Figure 3 displays a sequence of pictures for $F_r = V_0/\sqrt{gD} = 5.03$ from the experiment which illustrates the evolution of air cavity starting form initial formation until pinch-off. Detailed comparisons of the cavity profiles (for the case in figure 3) among the experimental data, theoretical prediction and fully nonlinear simulation are shown in figure 4. Excluding the spray which is hard to quantify from video images and to obtain accurately in the MEL panel method, the result from the nonlinear simulation agrees very well with the experimental data for the cavity shape and size, body position, as well as the cavity pinch-off location. (The comparison is somewhat less satisfactory near the pinch-off probably due to effects such as surface tension not included in the simulation.) The asymptotic solution captures the main features of the cavity, and agrees remarkably well with the numerical simulation and experimental data except near the body where the slender body assumption is poor. The asymptotic theory profiles are omitted near the free surface (or for small time)
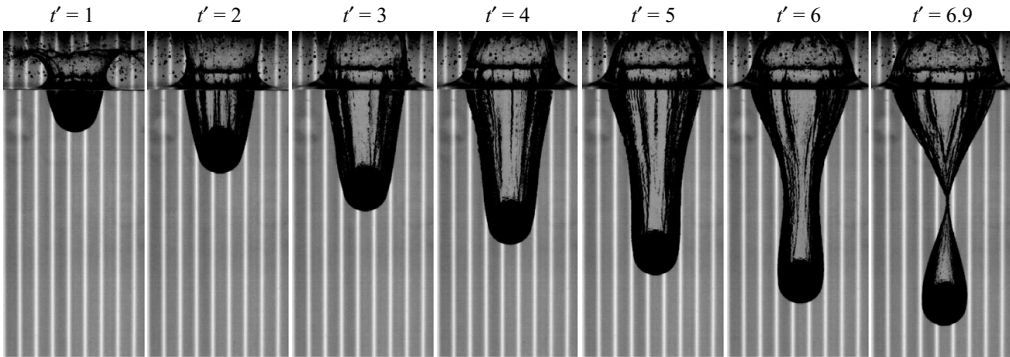
FIGURE 3. Time ($t' = tV_0/D$) evolution of an air cavity in water entry of a billiard ball at $F_r = 5.03$ from the experiment.
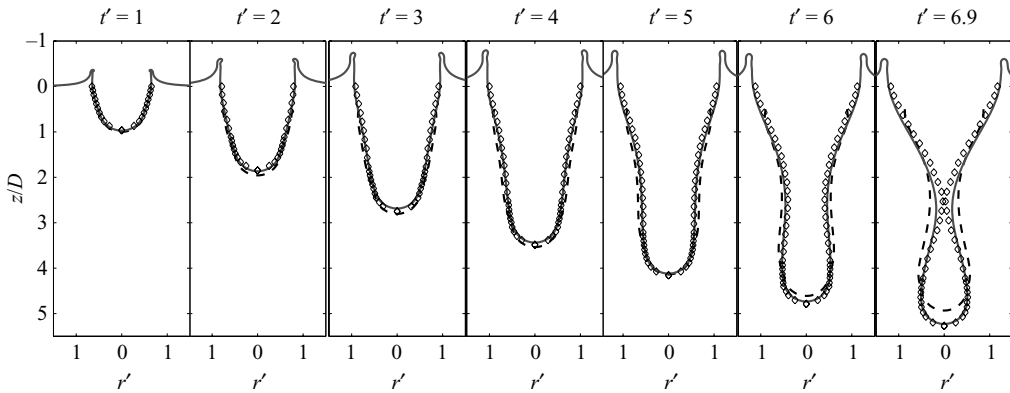

FIGURE 4. Comparisons of the cavity profile ($F_r = 5.03$) between experimental measurement ($\diamond$), numerical simulation (——) and asymptotic solution (- - -) at different time $t' = tV_0/D$.

here and in the following where the solution is invalid because splash effects are neglected (cf. 3.6)).

Figure 5 compares the position $z_b(t)$ of the freely falling sphere ($F_r = 5.03$) as a function of time until pinch-off T, obtained by the experiment, simulation and asymptotic theory. The agreements are excellent almost everywhere. For the asymptotic theory, $z_b(t)$ is slightly underpredicted. This is mainly due to the deficiency of the slender-body drag approximation (3.25), which as noted in §3.5, generally overpredicts the actual drag.

The radial position of the cavity wall $a(H_c, t)$ (at depth $z = H_c \approx 2.48D$ from the experiment) is compared in figure 6 for $t > t_0 \approx 2.74D/V_0$ (from figure 5, $z_b = H_c$ is reached at this time). The trajectory a is well predicted by the nonlinear simulation and in particular the time to reach R_m at $t = t_0 + \delta t_1 \approx 4.45D/V_0$. Consistent with figure 4, the comparison is not as good for later time $t \sim T (\approx 6.9D/V_0)$. The asymptotic theory consistently overpredicts a, with R_m overpredicted by about 9.3 %, although δt_1 seems to be well predicted. Considering the rather approximate estimate for σ in §3.2 (based on an assumption of the separation position), this is acceptable.

Figure 7 shows the maximum cavity size $R_m(z)$ reached at each depth. Our results indicate that $R_m(z)$ generally decreases with z for the cases we considered (with $V(t)$ non-increasing). This can be qualitatively obtained by considering the matched
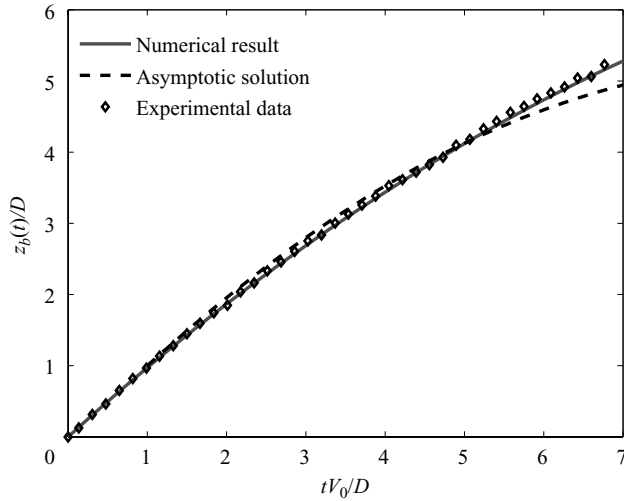
FIGURE 5. Trajectory of the freely falling sphere ($F_r = 5.03$) as a function of time: experimental measurement ($\diamond$), numerical simulation (——) and asymptotic solution (- - -).
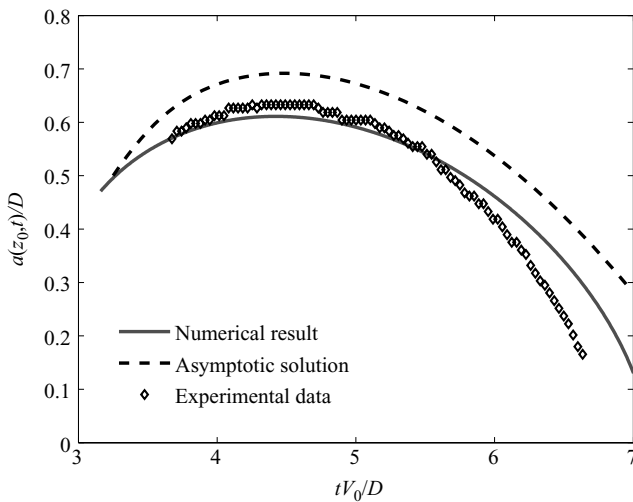

FIGURE 6. The radial trajectory of the cavity wall at $z_0 = 2.48D$ as a function of time ($F_r = 5.03$): experimental measurement ($\diamond$), numerical simulation (——) and asymptotic solution (- - -).

asymptotic solution. From § 3.4, the expanding radial velocity due to ϕ_b is counter-acted by the contracting radial velocity due to ϕ_c. The contribution due to the latter increases (in magnitude) with increasing depth z (see (3.19a)). Thus, in general $R_m(z)$ is smaller for greater z, for non-increasing $V(t)$ with time. If $V(t)$ is increasing, the expanding radial velocity $(\phi_b)_r$ also increases with time ((3.8) with $\sigma(t) = 2\pi R^2 V(t)$). On the other hand, the contracting radial velocity $(\phi_c)_r$ depends only weakly on $V(t)$ (through ϕ_b, for increasing z). The net effect as a function of z is therefore not definite and $R_m(z)$ may or may not be a decreasing function of z. The overall comparisons among the three results are again very satisfactory for a broad range of z up to $z \sim H$.
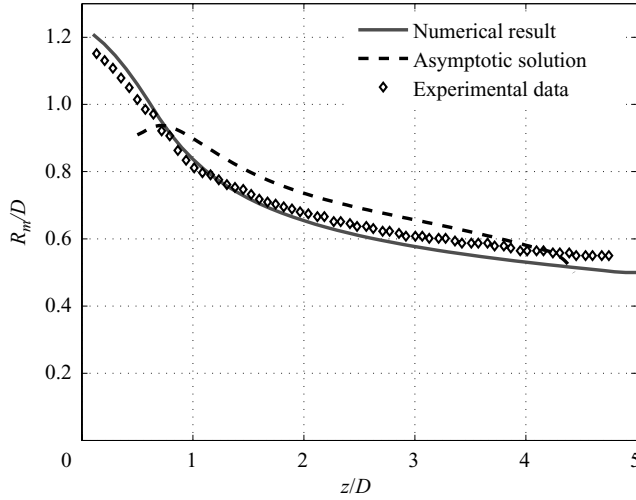
FIGURE 7. Maximum cavity radius as a function of depth ($F_r = 5.03$): experimental measurement ($\diamond$), numerical simulation (——) and asymptotic solution (- - -).
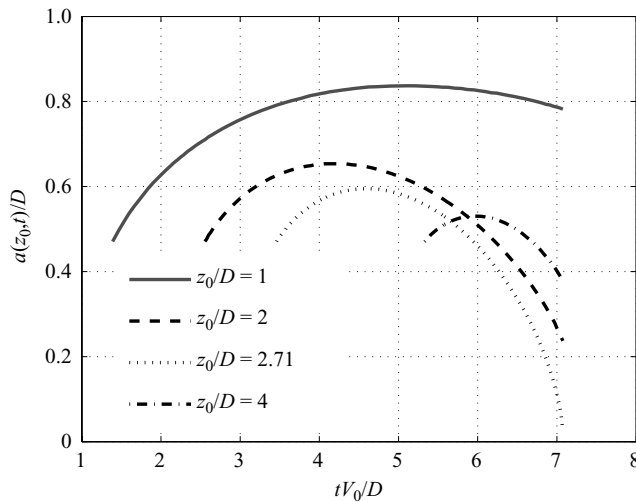

FIGURE 8. Time variation of the radial trajectory of cavity wall at depth $z_0/D = 1$ (——), 2 (- - -), 2.71 ($\cdots$) and 4 (- $\cdot$ -) obtained by fully nonlinear simulations ($F_r = 5.03$).

Figure 8 shows the numerical results for the radial trajectory $a(z_0, t)$ of the cavity wall at different depths z_0 from initial time $t = t_0(z_0)$ until cavity pinch off at $t = T(\approx 7.08D/V_0$ for this case). The profiles of $a(z_0, t)$ are similar for different z_0 and confirm the qualitative behaviour described in § 2.2. After the body passes z_0, $t > t_0(z_0)$, a increases, reaches a maximum $a = R_m$ at $t = t_0(z_0) + \delta t_1(z_0)$, and then decreases. Pinch-off occurs at some (intermediate) depth $z = H_c(\approx 2.71D)$ where a first reaches zero, as shown in the figure. $R_m(z_0)$ decreases with z_0 as discussed in figure 7. It is noteworthy that $a(z_0, t)$ is not symmetric in time with respect to $t = t_0(z_0) + \delta t_1(z_0)$ when $a = R_m$. This differs from prediction by two-dimensional models (Birkhoff & Zarantonello 1957; Lee *et al.* 1997), which predict symmetry with respect to the expansion and contraction phases.
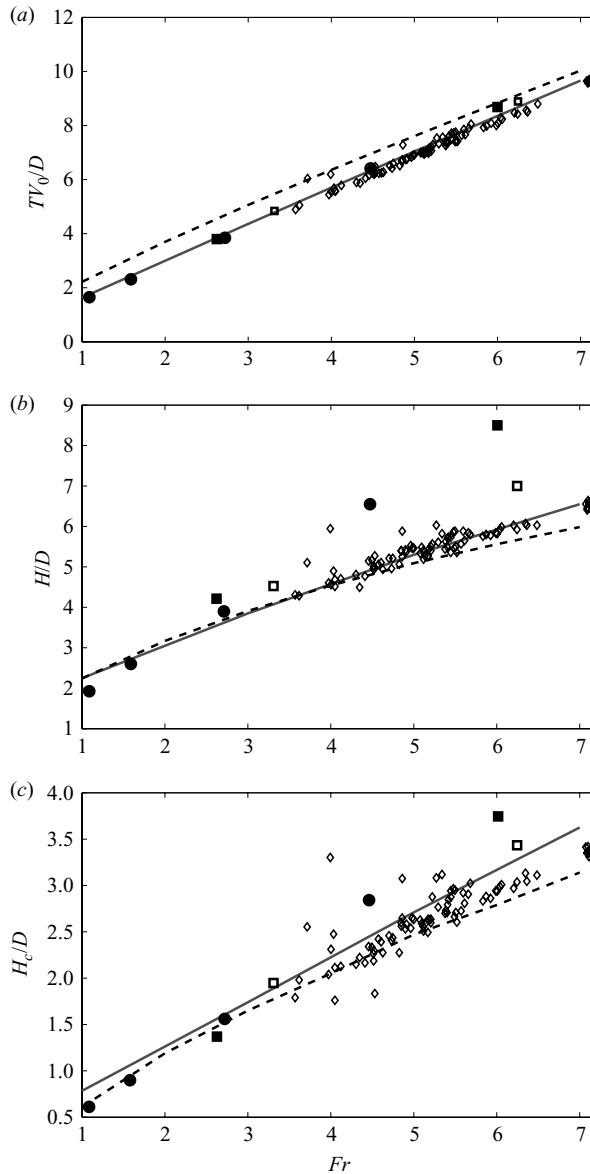
FIGURE 9. Dependence of (*a*) cavity closure time *T*, (*b*) total height of cavity *H* and (*c*) depth of cavity closure H_c on Froude number F_r: present experimental data ($\diamond$), experimental data of Duclaux *et al.* (2007) (sphere diameter $D = 12$ mm ($\blacksquare$), $D = 15.6$ mm ($\square$) and $D = 24$ mm ($\bullet$)), fully nonlinear simulation (—) and asymptotic solution (- - -).

Finally, we examine the dependence of cavity development on Froude number for the freely falling sphere. Figure 9 plots pinch-off time *T*, position H_c and total cavity height at pinch-off *H* for $F_r = 1 \sim 7$. We include for comparison also the measurements of Duclaux *et al.* (2007) (who use glass spheres of specific densities ranging from 2.36 to 7.74, relative to our value of $\rho_b/\rho \approx 1.73$). The results are generally in agreement especially for the dependence of dimensionless pinch-off time TV_0/D on F_r. As expected, for the higher density spheres of Duclaux *et al.* (2007) the values for H/D
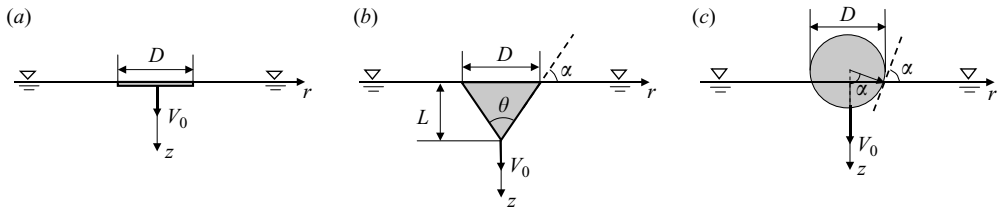
FIGURE 10. Schematic of the different (axisymmetric) geometries at the point of flow separation. The flow separation angle α used in the nonlinear simulations are (a) $\alpha = 0°$ for the disk; (b) $\alpha = 90° - \theta/2$ for the inverted truncated cone and (c) $\alpha = 70°$ prescribed for the sphere.
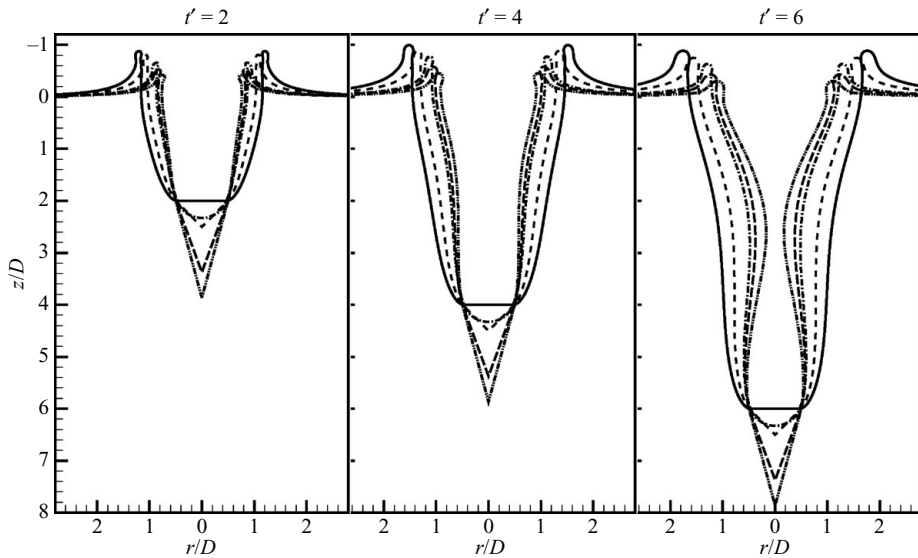

FIGURE 11. Cavity profiles in water entry of a disk (—), inverted truncated cones (height $L/D = 0.5$, $\theta = 90°$ (- - -); height $L/D = 2.75$, $\theta = 40°$ (– –); height $L/D = 3.73$, $\theta = 30°$ (- · · -)) and a sphere (- · -) with $F_r = 5$ at different time $t' = tV_0/D$. The results are obtained by fully nonlinear simulations.

and H_c/D are somewhat greater (especially for larger F_r) corresponding to greater (average) V/V_0. If we think of the Froude number in terms of the average V/V_0, then denser spheres have effectively greater Froude numbers, which explains the steeper slopes of the H/D and H_c/D versus F_r curves for denser spheres.

As observed by Duclaux *et al.* (2007) and others (e.g. Glasheen & McMahon 1996 for dropping disks) in experiments and by the numerical simulation of Gaudet (1998) (for the disk); and consistent with (two-dimensional) theories (e.g. Birkhoff & Zrantonello 1957; Lee *et al.* 1997); T, H_c and H are all approximately linear increasing functions of F_r. Our results capture this linear dependence with excellent comparison between the nonlinear simulation and measurements. The asymptotic solution predicts the slope but somewhat overpredicts the value of $T(F_r)$. The theory slightly underpredicts $H_c(F_r)$ and $H(F_r)$ especially for higher F_r. As pointed out in figures 6 and 7, the asymptotic theory overpredicts the drag force which (among other effects) delays the arrival of the body and evolution of the cavity.
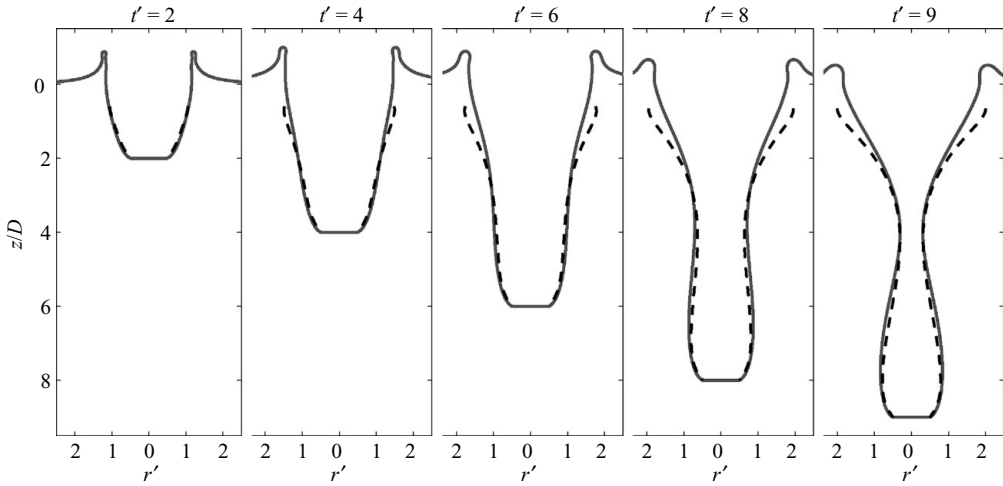
FIGURE 12. Comparison of the cavity shapes obtained by fully nonlinear simulation (——) and asymptotic analysis (- - -) in the water entry of a circular disk with $F_r = 5$ at different time $t' = tV_0/D$.
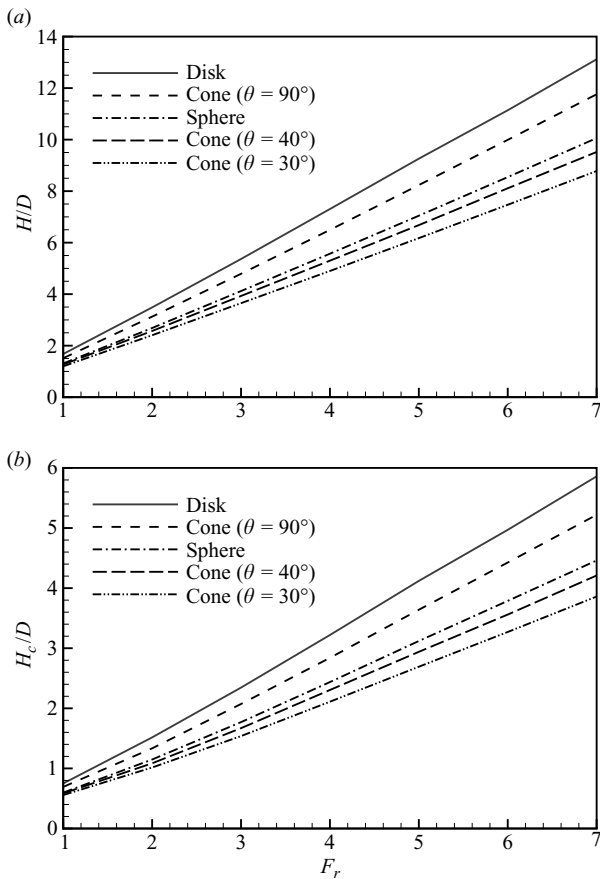

FIGURE 13. Fully nonlinear simulation results of (*a*) total cavity length (H) and (*b*) cavity closure depth (H_c) in water entry of a disk (——), inverted truncated cones (height $L/D = 0.5$, $\theta = 90°$ (- - -); height $L/D = 2.75$, $\theta = 40°$ (– –); height $L/D = 3.73$, $\theta = 30°$ (- · · -)) and a sphere (- · -).
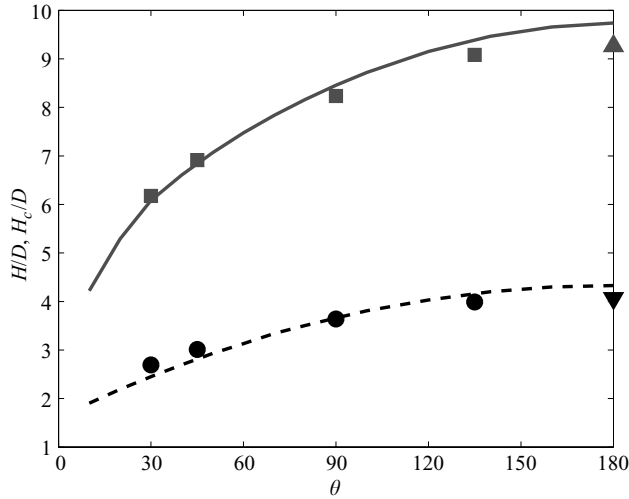
FIGURE 14. Dependence of total cavity length (H) and depth of pinch-off (H_c) on cone vertex angle θ for water entry of inverted truncated cones at $F_r = 5$. Plotted are the asymptotic prediction for H (—) and H_c (– –), numerical simulation result of H (■) and H_c (●) for the cones and H (▲) and H_c (▼) for the disk.

5.2. Body geometry effect

To understand the effect of body geometry, we conduct nonlinear numerical simulations for the cavity development behind a number of other shapes, specifically for circular disk and inverted truncated cones of different heights, and compare these to the sphere (see figure 10). For the numerics, flow separation is enforced at the sharp edges for the disk and inverted truncated cones. For simplicity we set imposed constant downward velocity V_0 in all cases.

Figure 11 compares the numerically obtained profiles of the cavity associated with water entry of the different bodies. As expected, the cavity lateral size (corresponding to the same time) increases with the bluffness of the body geometry, in particular with decreasing flow separation angles α. Note that the profiles for the inverted truncated cone of vertex angle $\theta = 40°$ ($\alpha = 70°$) is slightly narrower than that of the sphere (with the same value of α) due to the difference of the wetted body geometry.

For illustration, the asymptotic theory prediction is also shown and compared to numerical result for the case of the disk (figure 12). The comparison is excellent including near the body. Because of the neglect of splash effect, the asymptotic theory is invalid near the free surface (results are omitted).

Figure 13 compares the total cavity length $H (= T V_0)$ and closure depth H_c of different body geometries as functions of F_r. The linear dependencies observed earlier (for the sphere) obtain here. The slopes of the $H(F_r)$ and $H_c(F_r)$ curves increase with body bluffness. This qualitative behaviour of H and H_c increasing with body bluffness shown in figure 13 can be obtained from the asymptotic theory where the point source strength σ increases with bluffness. Larger σ strengthens the expansion phase of the cavity development and thus leads to greater H and H_c. Figure 14 shows the asymptotic theory prediction of H and H_c for a wide range of vertex angle θ for inverted truncated cones at $F_r = 5.0$. The asymptotic solution agrees well with the nonlinear simulation. H and H_c monotonically increase with θ as σ does.
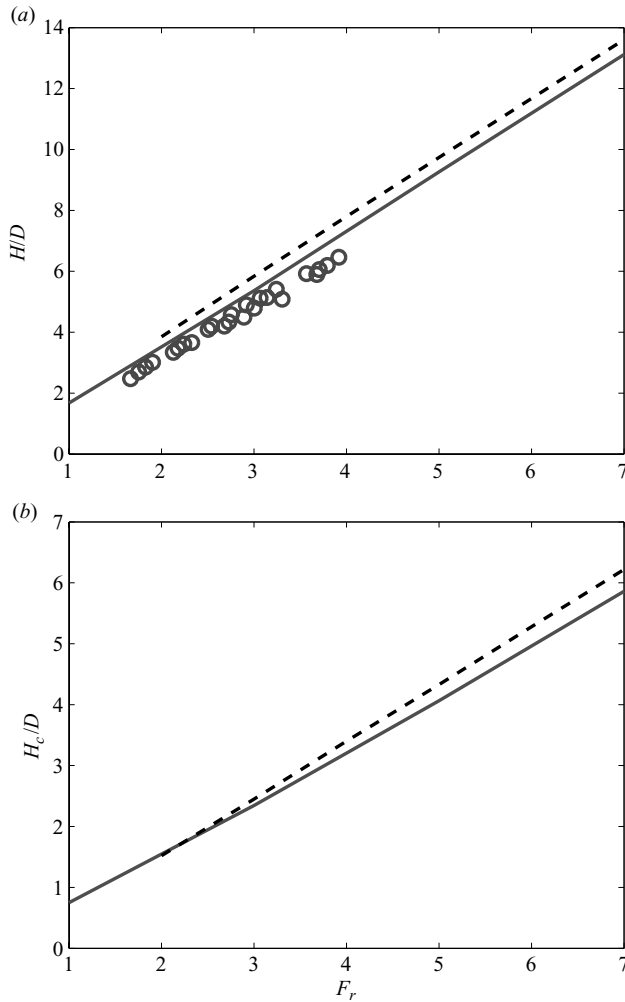
FIGURE 15. Comparisons of (*a*) total cavity height (*H*) and (*b*) depth of cavity closure (*H$_c$*) among the experimental data of Glasheen & Mcmahon (1996) (○), the fully nonlinear simulation result(—) and the asymptotic solution (- - -) for a disk with constant dropping velocity.

We remark here that from the (near) linear dependencies of H and H_c on F_r in figure 13 (and the fact that H and H_c vanish for $F_r \to 0$), it follows that H_c/H is (nearly) constant and independent of F_r for a given geometry (Lee *et al.* 1997; Duclaux *et al.* 2007; Bergmann *et al.*, private communication, 2009).

H and H_c as a function of F_r for the disk have been measured experimentally by Glasheen & McMahon (1996). Figure 15 compares the measurements with our numerical simulation and asymptotic theory prediction. The comparisons are quite satisfactory. Relative to the measurements, our results slightly overpredict H and H_c which can be explained by experimental deviation (decrease) of the drop velocity from V_0. Recently, Bergmann *et al.* (private communication, 2009) repeated the same measurements with carefully controlled constant $V = V_0$ which may remove such discrepancies.

6. Conclusions

We consider the hydrodynamic problem of air cavity development and evolution in vertical water entry of an axisymmetric body. The problem is studied using asymptotic analysis and fully nonlinear numerical simulations in the context of potential flow, and laboratory experiments. The focus is in the range of relatively low Froude number, $F_r \leqslant O(10)$, where gravity effects cannot be neglected. Using a matched asymptotic approach, we derive a theoretical solution for the description of the dynamics of the air cavity including three-dimensional body and flow effects. The asymptotic solution provides useful insights into the understanding of salient features and associated dynamics in the evolution of the air cavity. To validate and complement the asymptotic analysis, we develop a nonlinear numerical simulation which includes full body and nonlinear free-surface wave effects. Finally, we conduct a relatively limited set of experimental measurements using freely dropping spheres.

Satisfactory quantitative comparisons among the asymptotic theory predictions, nonlinear numerical simulations and the present and existing experimental measurements are obtained for the freely dropping sphere including predictions of the cavity shape, maximum radius, pinch-off position, closure time and closure height. To understand the effect of body geometry on cavity properties, we apply the matched asymptotic solution and numerical simulations to circular disk and inverted truncated cones. The asymptotic solution is found to be remarkably robust. For the disk, our analytical and numerical predictions agree well with available measurements.

These results underscore the importance of air cavity dynamics in bluff body water entry. The dynamics of the body differs significantly before and after cavity closure and depends critically on cavity closure parameters. In the low-Froude-number regime, in particular, depth of cavity closure and total cavity height increase linearly with the Froude number independent of body geometry. This study lays the foundation for understanding more general water impact/entry problems involving complex geometries, such as ship bow impact, projectile entry and animals running on water surface.

REFERENCES

ARISTOFF, J. M. & BUSH, J. W. M. 2009 Water entry of small hydrophobic spheres. *J. Fluid Mech.* **619**, 45–78.

BIRKHOFF, G. & ZARANTONELLO, E. H. 1957 *Jets, Wakes, and Cavities.* Academic Press.

CHU, P. C., FAN, C. W., EVANS, A. D. & GILLES, A. F. 2004 Triple coordinate transforms for prediction of falling cylinder through the water column. *J. Appl. Mech.* **71**, 292–298.

DOMMERMUTH, D. G. & YUE, D. K. 1987 Numerical simulations of nonlinear axisymmetric flows with a free surface. *J. Fluid Mech.* **178**, 195–219.

DUCLAUX, V., CAILLE, F., DUEZ, C., YBERT, C., BOCQUET, L. & CLANET, C. 2007 Dynamics of transient cavities. *J. Fluid Mech.* **591**, 1–19.

DUEZ, C., YBERT, C.,CLANET, C. & BOCQUET, L. 2007 Making a splash with water repellency. *Nature Phys.* **3**, 180–183.

GAUDET, S. 1998 Numerical simulation of circular disks entering the free surface of a fluid. *Phys. Fluids* **10** (10), 2489–2499.

GILBARG, D. & ANDERSON, R. A. 1948 Influence of atmospheric pressure on the phenomena accompanying the entry of spheres into water. *J. Appl. Phys.* **19** (2), 127–139.

GLASHEEN, J. W. & MCMAHON, T. A. 1996 Vertical water entry of disks at low Froude numbers. *Phys. Fluids* **8** (8), 2078–2083.

GREENHOW, M. 1988 Water-entry and -exit of a horizontal circular cylinder. *Appl. Ocean Res.* **10** (4), 191–198.

HOLLAND, K. T., GREEN, A. W., ABELEV, A. & VALENT, P. J. 2004 Parameterization of the in-water motions of falling cylinders using high-speed video. *Exp. Fluids* **37** (5), 690–700.

HULME, A. 1983 A ring source integral equation method for the calculation of hydrodynamic forces exerted on floating bodies of revolution. *J. Fluid Mech.* **128**, 387–412.

KOMINIARCZUK, J. K. 2007 Cavity and projectile dynamics in intermediate Froude number water entry. SB thesis, Massachusetts Institute of Technology, Cambridge, MA.

KOROBKIN, A. A. & PUKHNACHOV, V. V. 1988 Initial stage of water impact. *Annu. Rev. Fluid Mech.* **20**, 159–185.

LAERM, J. 1974 A functional analysis of morphological variation and differential niche utilization in basilisk lizards. *Ecology* **55**, 404–411.

LEE, M., LONGORIA, R. G. & WILSON, D. E. 1997 Cavity dynamics in high-speed water entry. *Phys. Fluids* **9** (3), 540–550.

LIN, M. C. & SHIEH, L. D. 1997 Simultaneous measurements of water impact on a two-dimensional body. *Fluid Dyn. Res.* **19**, 125–148.

LIU, Y., XUE, M., & YUE, D. K. 2001 Computations of fully nonlinear three-dimensional wave-wave and wave-body interactions. Part 2. Nonlinear waves and forces on a body. *J. Fluid Mech.* **438**, 41–66.

LOHSE, D., BERGMANN, R., MIKKELSEN, R., ZEILSTRA, C., VAN DER MEER, D., VERSLUIS, M., VAN DER WEELE, K., VAN DER HOEF, M. & KUIPERS, H. 2004 Impact on soft sand: void collapse and jet formation. *Phys. Rev. Lett.* **93** (19), 198003.

MANN, J. L. 2005 Deterministic and stochastic modeling of the water entry and descent of three-dimensional cylindrical bodies. MS thesis, Massachusetts Institute of Technology, Cambridge, MA.

MANN, J. L., LIU, Y., KIM, Y. & YUE, D. K. P. 2007 Deterministic and stochastic predictions of motion dynamics of cylindrical mines falling through water. *IEEE J. Ocean Engng* **32** (1), 21–33.

MAY, A. 1951 Effect of surface condition of a sphere on its water-entry cavity. *J. Appl. Phys.* **22** (10), 1219–1222.

MAY, A. 1952 Vertical entry of missiles into water. *J. Appl. Phys.* **23** (12), 1362–1372.

MAY, A. & WOODHULL, J. C. 1948 Drag coefficients of steel spheres entering the water vertically. *J. Appl. Phys.* **19**, 1109–1121.

MEI, C. C., STIASSNIE, M., & YUE, D. K. 2005 *Theory and Applications of Ocean Surface Waves, Part 1: Linear Aspects.* World Scientific.

NEWMAN, J. N. 1977 *Marine Hydrodynamics.* MIT Press.

RICHARDSON, E. G. 1948 The impact of a solid on a liquid surface. *Proc. Phys. Soc.* **61**, 352–367.

TRUSCOTT, T. T. & TECHET, A. H. 2009 Water-entry of spinning spheres. *J. Fluid Mech.* **625**, 135–165.

VAN DYKE, M. 1964 *Perturbation Methods in Fluid Mechanics.* Academic Press.

WANG, Q. X. 2004 Numerical simulation of violent bubble motion. *Phys. Fluids* **16** (5), 1610–1619.

WANG, Q. X. 2005 Analyses of a slender body moving near a curved ground. *Phys. Fluids* **17** (9), 097102.

WANG, Q. X. 2007 An analytical solution for two slender bodies of revolution translating in very close proximity. *J. Fluid Mech.* **582**, 223–251.

WORTHINGTON, A. M. & COLE, R. S. 1900 Impact with a liquid surface studied by the aid of instantaneous photography. Paper II. *Phil. Trans. R. Soc. Lond.* A **194**, 175–199.

XUE, M. & YUE, D. K. 1998 Nonlinear free-surface flow due to an impulsively started submerged point sink. *J. Fluid Mech.* **364**, 325–347.